Supplementary Table 1. Definition of parameters.

Parameter	Description	Useful relation
L	Length of a nanobender	
t	Thickness of a nanobender	
w	Width of a nanobender	
C	Bending curvature of a nanobender	
ϕ	Central angle of a deformed nanobender	
θ	Deflection angle at the end of a deformed nanobender	$\theta = \phi/2 = CL/2$
Δ	Displacement at the end of a deformed nanobender	$\Delta = L\theta = CL^2/2$
w_{m}	Width of the metal electrodes	
w_{g}	Gap between the metal electrodes	
t_{m}	Thickness of the metal electrodes	
$\tilde{g}$	Shortest distance between the two zipper beams	
$\tilde{g}_0$	Initial gap size	
G_{OM}	Opto-mechanical coupling	$G_{\mathrm{OM}} = \partial\omega_0/\partial z$
α	DC tuning coefficient of the bender-zipper cavity	$\alpha = d\lambda/dV\|_{V=0}$
Ω	Modulation frequency in the AC tuning measurement	
V_{dc}	Bias voltage in the AC tuning measurement	
V_{ac}	Modulation voltage in the AC tuning measurement	
Δ_{dc}	Wavelength change from the bias voltage	$\Delta_{\mathrm{dc}} = \alpha V_{\mathrm{dc}}$
Δ_{ac}	Wavelength change from the modulation voltage	
α_{ac}	AC tuning coefficient	$\alpha_{\mathrm{ac}} = \Delta_{\mathrm{ac}}/V_{\mathrm{ac}}$

Nanobenders as efficient piezoelectric actuators for widely tunable nanophotonics at CMOS-level voltages: supplementary information

Wentao Jiang, Felix M. Mayor, Rishi N. Patel, Timothy P. McKenna, Christopher J. Sarabalis, and Amir H. Safavi-Naeini

Supplementary Note 1. DERIVATION OF THE DISPLACEMENT OF ONE NANOBENDER

Here we derive an approximate theory for the nanobenders. The quadratic scaling law between displacement and length of the nanobender is derived. For clarity, we have listed relevant parameters in Supplementary Table 1.

Supplementary Figure 1 shows a single nanobender at equilibrium in dashed black and after deformation in solid black. The left end of the nanobender at $x = 0$ is fixed. We tailor the following discussion for application to lithium niobate (LN), thus the coordinate system is chosen to coincide with the material coordinate system of LN. The right end at $x = L$ bends towards the positive z direction by Δ when a non-uniform electric field $\boldsymbol{E}(\boldsymbol{r})$ is applied and generates a displacement field $\boldsymbol{u}(\boldsymbol{r})$. A small angle θ, shown as green dashed lines, is formed by the equilibrium and deformed right end of the nanobender, and the fixed left end. We consider an electric field that is parallel to the y direction (out-of-plane), homogeneous along x and y, and varies linearly along the z direction (perpendicular to the nanobender). Consequently, the electric field can be written as $E_y(z) = z \cdot \partial_z E_y$, where $\partial_z E_y$ is spatially homogeneous. We have ignored the effect of a constant electric field which induces a homogeneous strain field, and the generated displacement at the end of the beam is at most proportional to its length L.

Bending of the beam can be well described by a radius R and the corresponding curvature $C \equiv 1/R$ when $R \gg L$. The contraction and expansion on the two sides of the beam are related to the bending radius as

$$(R - w/2)\phi = L + u_x(x = L, z = w/2), \tag{1}$$

$$(R + w/2)\phi = L + u_x(x = L, z = -w/2), \tag{2}$$

where u_x is the x component of the $\boldsymbol{u}$ field, w is the width of the beam and ϕ is the corresponding central angle of the deformed beam. Subtracting the two equations, we obtain

$$\phi = -\partial_z u_x|_{x=L} = -L\partial_z S_{xx} = -d_{21} L \partial_z E_y, \tag{3}$$

$$\implies C = \phi/L = -d_{21}\partial_z E_y. \tag{4}$$

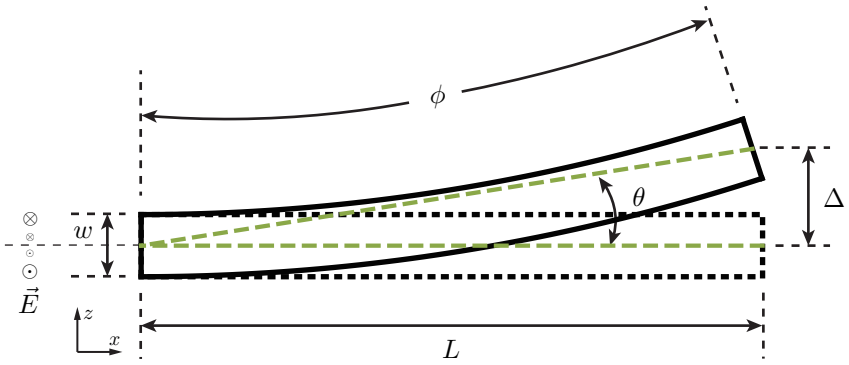

Supplementary Figure 1. **Schematic drawing of a bending beam.** The material coordinate system is chosen and labeled with x, y, z. In the case of LN nanobenders, this represents either the side view or the top view of a nanobender, depending on the crystal cut. The direction and spatial variation of the $\boldsymbol{E}$ field is shown on the left.

The resulting deflection angle θ and the deflection Δ along the z direction are given by

$$\theta = \frac{\phi}{2} = -\frac{1}{2} d_{21} L \partial_z E_y = \frac{1}{2} C L, \tag{5}$$

$$\Delta \approx L\theta = -\frac{1}{2} d_{21} L^2 \partial_z E_y = \frac{1}{2} C L^2. \tag{6}$$

We would like to point out that the actual displacement could be either in-plane if Y-cut LN is chosen such that the surface of the chip is perpendicular to y, or out-of-plane on Z-cut LN, where the surface of the chip is perpendicular to z, so long as $\partial_z E_y$ is generated by the electrode configuration. In addition, the above discussion holds for any piezoelectric material with a non-vanishing transverse piezoelectric coefficient.

More generally, the non-uniform electric field can be approximated to first order as

$$E_y(y, z) = y \cdot \partial_y E_y + z \cdot \partial_z E_y. \tag{7}$$

The spatially uniform component of the field is ignored. The electrodes for generating the $\boldsymbol{E}$ field are assumed to have a translational symmetry along the direction of the beam (x-axis), thus the E_x component is negligible. Furthermore, the magnitude of LN's d_{21} is more than one order of magnitude larger than the other non-zero transverse piezoelectric coefficients. Therefore, we only consider the d_{21} piezoelectric component and the only relevant electric field component is E_y. The validity of this approximation is confirmed by simulations in Supplementary Note 2 A.

The full piezoelectric constitutive equations in the strain-charge form are

$$\boldsymbol{S} = \boldsymbol{s}_E \boldsymbol{T} + \boldsymbol{d}^T \boldsymbol{E}, \tag{8}$$

$$\boldsymbol{D} = \boldsymbol{d}\boldsymbol{T} + \boldsymbol{\epsilon}_T \boldsymbol{E}, \tag{9}$$

where $\boldsymbol{s}_E$ is the compliance matrix, $\boldsymbol{\epsilon}_T$ is the unclamped permittivity, $\boldsymbol{D}$ is the electric displacement and $\boldsymbol{T}$ is the stress. For a nanobender anchored on one end under one volt applied voltage, the stress in the body of the beam is typically $\sim 10^6$ Pa from simulation. The compliance of LN is $s_E \approx 5 \times 10^{-12}$ Pa^{-1}, thus $s_E T \sim 5 \times 10^{-6}$. On the other hand, the electric field $E \sim 1$ V/(200 nm) $= 5 \times 10^6$ V m^{-1} while $d \approx 2 \times 10^{-11}$ m V^{-1}, leading to $d \cdot E \sim 10^{-4}$. As a consequence, Eq. 8 can be well approximated by $\boldsymbol{S} = \boldsymbol{d}^T \boldsymbol{E}$. This observation agrees with the intuition one would have for a mostly free beam, where the internal stress is expected to be small. Larger stress is localized near the surface of the beam at the boundary of the electrodes, where the electric boundary condition is not continuous.

The displacement field can be solved from the strain field $S_{xx}(y, z) = d_{21} E_y(y, z)$ and $S_{ij} = 0$ for all other components. For a free beam with $\boldsymbol{u}(0, 0, 0) = (0, 0, 0)$ and ignoring any rigid rotation,

$$\boldsymbol{u}(x, y, z) = d_{21} \left(x(y\partial_y E_y + z\partial_z E_y), -\frac{1}{2} x^2 \partial_y E_y, -\frac{1}{2} x^2 \partial_z E_y \right), \tag{10}$$

$$\Delta \equiv u_z(x = L) = -\frac{1}{2} d_{21} L^2 \partial_z E_y = \frac{1}{2} C L^2. \tag{11}$$

As a result, bending of the beam is observed for both y and z direction, where the displacement at $x = L$ scales quadratically with the length of the beam L. The displacement along the z direction is identical to Eq. 6.

In the above derivation, $\partial_y E_y$ and $\partial_z E_y$ are assumed to be uniform on the cross-section of the beam. In reality for a Y-cut nanobender where a parallel pair of electrodes is placed on the top surface (x-z plane) of the beam, the

fringing field has a complicated spatial variation. Nevertheless, the field E_y mostly varies along the z direction and the variation along y is negligible after averaging over the cross section. Similarly, the field E_z mostly varies along the y direction. We verify this by numerically evaluating the average of $\partial_i E_j$ on the cross section for $i, j = y, z$ using COMSOL simulations. The averaged $\partial_y E_y$ and $\partial_z E_z$ are two orders of magnitude smaller than $\partial_y E_z$ and $\partial_z E_y$. This can be qualitatively understood by considering the symmetry of the electrostatic potential and the electric field. The parallel pair of electrodes possess z-reflection symmetry, where the geometry of the electrodes is invariant under reflection with respect to the symmetry plane $z = 0$. When a voltage difference is applied to the electrodes and by setting the potential reference such that $V = 0$ on $z = 0$, we have approximately $V(y, -z) \approx -V(y, z)$. Consequently,

$$\partial_y E_z(y, -z) \approx \partial_y E_z(y, z), \tag{12}$$
$$\partial_z E_y(y, -z) \approx \partial_z E_y(y, z), \tag{13}$$
$$\partial_y E_y(y, -z) \approx -\partial_y E_y(y, z), \tag{14}$$
$$\partial_z E_z(y, -z) \approx -\partial_z E_z(y, z). \tag{15}$$

The implication from these observations is that $\partial_y E_y$ and $\partial_z E_z$ average to roughly zero on the cross section. Intuitively speaking, by virtually dividing the beam into two halves separated by the z-symmetry plane, the two halves of the beam tend to bend against each other when $\partial_y E_y$ and $\partial_z E_z$ are considered, thus cancelling and leading to an insignificant deformation of the full beam. In contrast, they bend in accordance with each other from $\partial_y E_z$ or $\partial_z E_y$, generating a much larger bending of the full beam. Similarly for a Z-cut nanobender where the electrodes are fabricated on the x-y plane, y-reflection symmetry can be considered, and the same arguments still hold.

As discussed above, the bending from Eq. 10 is mostly along a single direction z, generating a "clean" displacement $\Delta \equiv u_z(x = L)$. In other words, for a nanobender where only d_{21} is considered as non-zero and the cross-section is symmetric under y or z reflection, the bending generates a displacement along the z direction.

For example, on a $Y(Z)$-cut LN nanobender, the displacement is mostly in-plane (out-of-plane) where displacements along the other directions are more than one order of magnitude smaller (see Supplementary Note 2 for simulation results). The largest contribution to displacements along the other directions is bending generated by a different transverse piezoelectric coefficient.

Lastly we would like to point out that the transverse piezoelectric coefficients (d_{13}-type) are not the only components that could potentially generate bending from a non-uniform electric field. Through numerical simulation (Supplementary Note 2), we found that the diagonal components (d_{11}-type) and the shear components (d_{14}-type) are also capable of generating bending under the parallel-pair electrode configuration.

Supplementary Note 2. SIMULATION OF ONE-VOLT DISPLACEMENT

We use the Piezoelectric Devices module in COMSOL for simulating the 3D model of the nanobender. A rotated coordinate system is adopted to account for different crystal cuts and nanobender orientations. A fixed constraint is applied to one end of the nanobender while the other surfaces are subject to a free boundary condition. The metal surfaces are selected and assigned as either ground or a voltage terminal with $V_0 = 1\,\mathrm{V}$. The full geometry is encapsulated in air for the electrostatics simulation. We found that the air encapsulation causes only a minor effect due to LN's large relative permittivity. A stationary study is solved for the static displacement, and an eigenfrequency study is solved for the eigenmode frequencies of the nanobender.

For generality and simplicity, from now on we adopt a global coordinate system, with axes denoted by x, y and z that are fixed with the nanobender, where x is parallel to the nanobender and is pointing from the fixed-end to the free-end. Positive z axis is perpendicular to the chip. We report the simulated displacements in this global coordinate system. As a result, for nanobenders parallel to crystal X axis as discussed above, the bending is always towards the crystal Z axis. The cut of the crystal is defined as the crystal axis perpendicular to the plane of the thin film from which the beam is fashioned. Since we often put electrodes on top of the thin film, the example in Supplementary Note Supplementary Note 1 would naturally correspond to a Y-cut film where the beam is patterned to be parallel to the crystal X. In the newly defined chip coordinate system, we have $z||Y$, $x||X$, $y||Z$, and therefore a large displacement being generated in $y(Z)$ which is in the plane of the chip. Similarly, for Z-cut nanobenders, a vertical bending results and leads to a large u_z.

A. Contributing piezoelectric components to the displacement

To show that the dominant contribution of the displacement is from the d_{21} component of the piezoelectric tensor, we conduct finite element simulations with the original piezoelectric tensor $\boldsymbol{d}$ and compare the results to simulations

where all components of $\boldsymbol{d}$ other than d_{21} are set to zero.

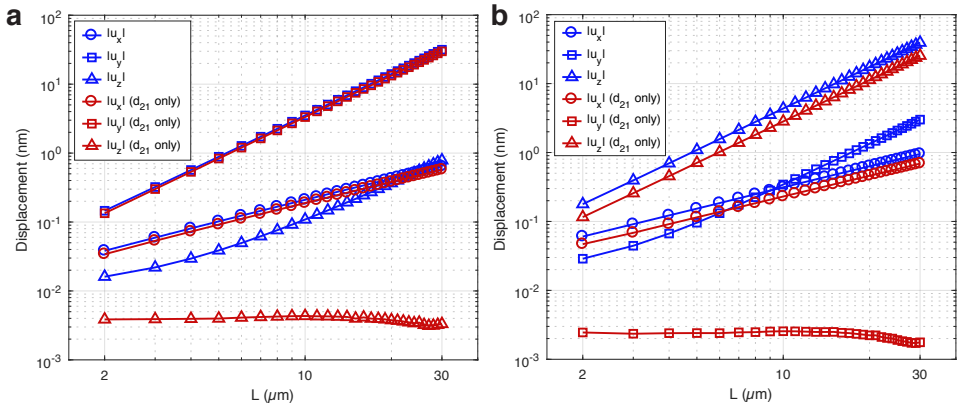

Supplementary Figure 2. **Simulated displacements** for Y-cut (**a**) (corresponding to Fig Supplementary Figure 1 with $\Delta = u_y$) and Z-cut (**b**) nanobenders ($\Delta = u_z$). To show the contribution from the d_{21} piezoelectric coefficient, identical geometry is simulated with full $\boldsymbol{d}$ tensor (blue) as well as a $\boldsymbol{d}$ tensor where d_{21} is the only non-zero component (red).

The simulated displacements are plotted in Supplementary Figure 2 for different nanobender lengths L in log scale. For Y-cut nanobenders (Supplementary Figure 2a), the d_{21} component is able to produce the simulated displacement from the full $\boldsymbol{d}$ tensor with minor deviation. The quadratic scaling of u_y versus L can be clearly observed by comparing to u_x. The large deviation between d_{21} only and full $\boldsymbol{d}$ simulations for u_z can be explained by the non-zero d_{31} component of LN, which generates out-of-plane bending from $\partial_y E_z$. Since the magnitude of d_{31} is more than one order of magnitude smaller than d_{21}, the vertical bending is negligible comparing to in-plane bending. However, the quadratic scaling is still present and makes u_z larger than u_x for sufficiently large L.

As for vertical nanobenders on Z-cut LN, we observe (Supplementary Figure 2b) that keeping only the d_{21} coefficient underestimates the full simulated displacement. The other piezoelectric components contribute to roughly 35% of the displacement u_z. Surprisingly we find that 29% out of the 35% displacement that cannot be explained by the d_{21} component originates from the d_{22} and d_{24} components. These components are not expected to generate bending from the intuitive explanation provided in Supplementary Note 1, and likely result from the complicated non-uniform electric field profile.

B. Dependency of displacement on nanobender geometry

So far, we have mostly considered the quadratic length-displacement relationship of the nanobender. Here, we investigate how other geometric parameters affect the displacement for both Y-cut and Z-cut nanobenders. Supplementary Figure 3a and b show how the maximal displacement of the nanobender for all three directions scales with width w and thickness t. As expected, the displacement increases for smaller width. We also observe that for varying thickness, the in-plane displacement u_y peaks at around $t = 300$ nm for a fixed electrode thickness $t_\mathrm{m} = 50$ nm. Furthermore, it is interesting to see how scaling the cross-section for a fixed length L =10 µm affects displacement. Scaling the cross-section relative to $(w, t, t_\mathrm{m}) = (450, 300, 50)$ nm, we observe (Supplementary Figure 3c) that as the cross-section increases, u_y and u_z decrease quadratically whereas u_x decreases linearly. Finally, following the scale-invariance argument in the main text, the displacement of the nanobender is not dependent on its relative size. By scaling the whole geometry of the nanobender relative to $(w, t, t_\mathrm{m}, L) = (450, 300, 50, 10^4)$ nm, we confirm through simulations that the displacement is indeed independent of geometry scaling.

For Z-cut nanobenders (Supplementary Figure 4), the simulations and analysis are similar except that the out-of-plane displacement component u_z is dominant instead of u_y.

Supplementary Note 3. CONTRIBUTION OF THE FLEXOELECTRIC EFFECT

The piezoelectric effect describes coupling between an electric field and strain through a linear relationship. It is described by a third-rank tensor $\boldsymbol{d}$. It is only present in some non-centrosymmetric crystals like lithium niobate.

The flexoelectric effect, on the other hand, couples an inhomogeneous strain to an electric field or conversely, an inhomogeneous electric field to a homogeneous strain. It is described by a fourth-rank tensor $\boldsymbol{\mu}$ and is present in

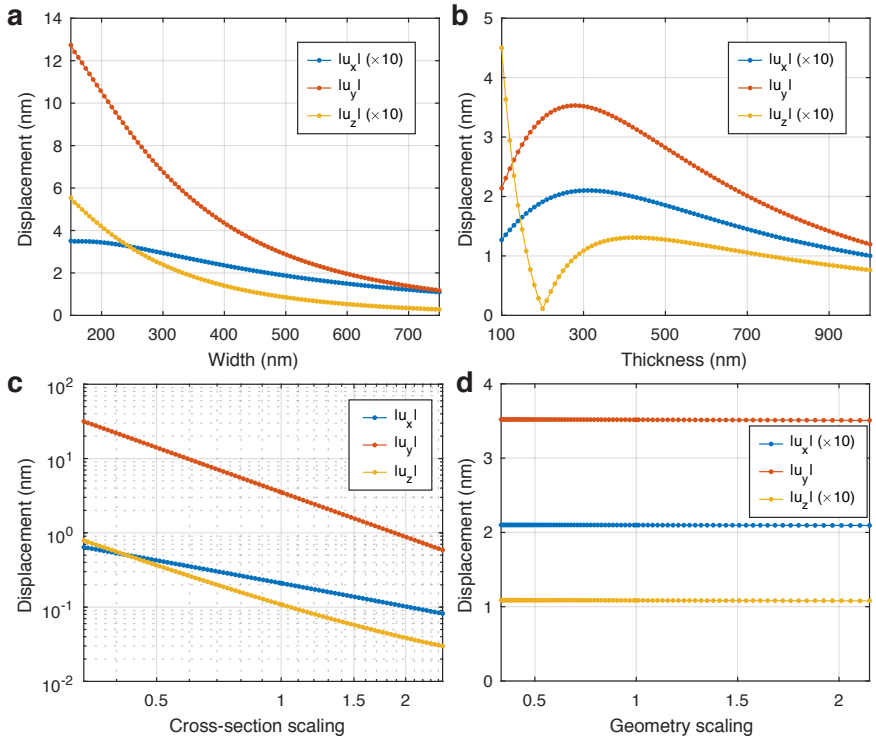

Supplementary Figure 3. **Simulated one-volt displacement for Y-cut nanobenders of varying geometries.** **a**, Sweep of the width w. **b**, Sweep of the thickness t. **c**, Scaling of the cross-section. **d**, Scaling of the whole geometry.

materials of all symmetry. Taking the piezoelectric constitutive equation for strain (Eq. 8): $\boldsymbol{S} = \boldsymbol{s}_E\boldsymbol{T} + \boldsymbol{d}^T\boldsymbol{E}$. Here, $\boldsymbol{s}_E$ is the compliance and $\boldsymbol{T}$ the stress. If the electric field is inhomogeneous (i.e. the spatial gradient $\nabla\boldsymbol{E} \neq 0$), then the strain S will also be inhomogeneous. In our case, this leads to bending (Fig. 1b & c in the main manuscript).

If we add the flexoelectric effect [1] to the constitutive equation above, we obtain

$$\boldsymbol{S} = \boldsymbol{s}_E\boldsymbol{T} + \boldsymbol{d}^T\boldsymbol{E} + \boldsymbol{s}_E\boldsymbol{\mu}\nabla\boldsymbol{E}. \tag{16}$$

This equation contains contributions from both the piezoelectric effect and flexoelectric effect. For a constant electric field gradient, the flexoelectric effect leads to a homogeneous strain. As we show below, in the case of the nanobender, the contribution of the piezoelectric effect overwhelmingly dominates over the flexoelectric effect.

To show this, we need to be able to isolate both contributions. As a comparison, we will be using reference [2]. There, the flexoelectric effect is used to bend a cantilever of strontium titanate, a centrosymmetric material (that is, not piezoelectric). They measure a flexoelectric coefficient $\mu = 4\,\mathrm{nC\,m^{-1}}$. Lithium niobate is piezoelectric and its flexoelectric coefficient is $\mu = 11\,\mathrm{nC\,m^{-1}}$ [3]. The two materials thus have similar flexoelectric coefficients and the contribution to strain is linear in μ.

The one-volt flexoelectric curvature measured by [2] is $C \sim 50\,\mathrm{m^{-1}}$ for a cantilever with thickness $t = 70$ nm. However, for a fair comparison, we need to scale the thickness of the cantilever up to $t = 450$ nm which corresponds to the nanobender width. Because $C \propto t^{-3}$ (equation 1 in [2]), the rescaled curvature is $C = (70/450)^3 \cdot 50\,\mathrm{m^{-1}} = 0.2\,\mathrm{m^{-1}}$.

Hence, the flexoelectric curvature we expect for the nanobender is more than two orders of magnitude smaller than the curvature generated by piezoelectricity. The curvature we found for the nanobender through piezoelectric simulations is $C \sim 100\,\mathrm{m^{-1}}$. This number is also confirmed by measurements. We can therefore entirely neglect the flexoelectric effect.

Supplementary Note 4. NANOPHOTONIC ZIPPER CAVITY DESIGN AND PROPERTIES

A. Mirror cell design

In the following, we briefly describe the procedure, adapted from Ref. [4], for designing the Y-cut lithium niobate mirror cell used as part of the 1D zipper nanophotonic cavity and the reflector at the end of the coupling waveguide.

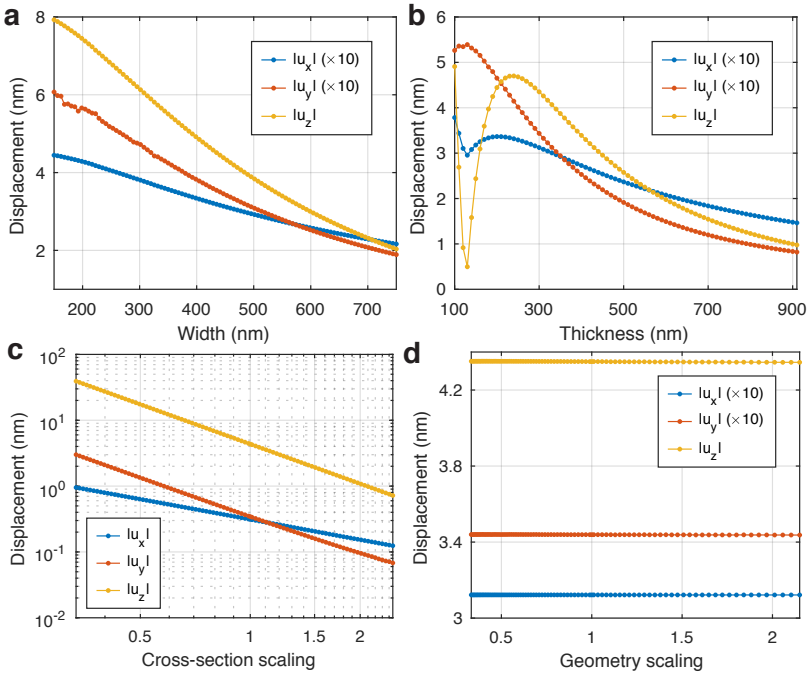

Supplementary Figure 4. **Simulated one-volt displacement for Z-cut nanobenders of varying geometries.** **a**, Sweep of the width w. **b**, Sweep of the thickness t. **c**, Scaling of the cross-section. **d**, Scaling of the whole geometry.

The thickness of the mirror cell is set to $t = 300$ nm. Because of fabrication imperfections, the LN structures have angled sidewalls which we take into account in the design. We therefore use an outer angle (defined as the angle between the sidewall and the vertical direction) of 11° and inner angle (inside the hole) of 22°, based on scanning electron micrographs. The mirror cell geometry (Supplementary Figure 5a) consists of two identical halves separated by a gap $\tilde{g}_0$. Each half is constructed by adding a cosine edge with amplitude $(w_2 - w_1)/4$ to a rectangle with dimensions a by $(w_1 + w_2)/2$. Half of an ellipse (with axes h_x and h_y) is then cut out of the rectangle to generate an air-hole. By periodically continuing the unit cell with lattice spacing a, we can open a quasi-transverse electric (TE) optical bandgap at the X-point (see Supplementary Figure 5b). Based on eigenfrequency simulations and optimization of the bandgap size, we choose the parameters $(a, w_1, w_2, h_x, h_y) = (650, 1395, 1007, 481, 1103)$ nm leading to a quasi-bandgap of 24.3 THz centered at 196.3 THz. We used multivariable genetic optimization to determine the parameters for this geometry. The cost function tries to maximize the size of the quasi-TE bandgap at the X-point while trying to push up the fundamental quasi-TM mode out of the bandgap to avoid scattering into it. The gap $\tilde{g}_0$ is set to 94 nm.

B. 1D nanophotonic zipper cavity

To localize an optical mode inside a 1D nanophotonic cavity, it is standard to introduce a defect unit cell inside an array of mirror cells with a smooth set of transition cells in between. This defect cell has a fundamental quasi-TE mode at the X-point that is inside the bandgap of the mirror cell. To generate the defect cell starting from the mirror cell, it is thus necessary to push up the fundamental quasi-TE mode of the mirror cell. This is achieved by reducing its lattice spacing a as well as the relative air-hole size. The defect and mirror cells are smoothly connected through cubic interpolation [5] using 12 transition cells (see Supplementary Figure 5c). We additionally have 8 mirror cells on each side of the cavity.

We determine the geometry of the defect cell with a similar multivariable genetic optimization. The cost function maximizes the optical quality factor Q of the localized fundamental optical mode while disregarding solutions that lead to unphysically high Qs [4]. As a result of this optimization, a defect cell geometry with parameters $(a, w_1, w_2, h_x, h_y) = (547, 1395, 1329, 381, 843)$ nm is chosen, and the number of transition cells and mirror cells are determined to be 12 and 8 respectively. Supplementary Figure 5d shows the simulated fundamental quasi-TE mode profile for this design choice. Furthermore, we see that the resonance wavelength of the cavity is strongly dependent on the gap $\tilde{g}_0$ of the cavity (Supplementary Figure 5e) leading to a large optomechanical coupling for the fundamental in-plane mechanical

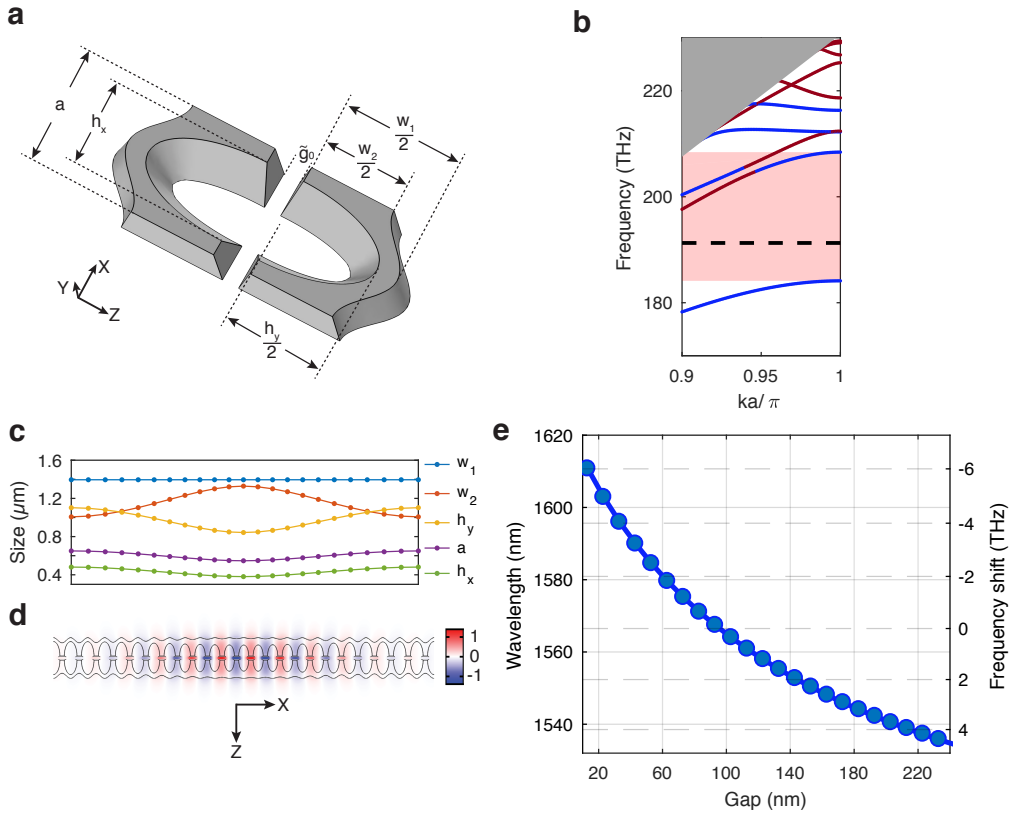

Supplementary Figure 5. **Nanophotonic zipper cavity design and properties.** **a**, Unit cell geometry of the lithium niobate zipper cavity. **b**, Optical band diagram of the unit cell geometry. The dashed line indicates the localized fundamental transverse electric optical mode. The grey region corresponds to the radiation continuum. **c**, Zipper cavity unit cell parameters along the transition from mirror cell to defect cell and back. **d**, Normalized E_Z component of the fundamental optical mode of the zipper cavity. **e**, Resonance wavelength versus zipper gap $\tilde{g}_0$.

mode of the bender-zipper structure.

C. Displacement of the bender-zipper cavity

In this section, we simulate the displacement of the bender-zipper cavity. Since the nanobender is only part of the full device, the displacement at the center of the zipper cavity is no longer simply given by a quadratic relationship. Moreover, we study how a tether with narrow width, added between the zipper cavity and the nanobender, could partially relax the zipper cavity - nanobender boundary condition from cantilevered to simply supported. The tether would effectively allow a local change of direction between the zipper cavity and the nanobender.

We simulate the full bender-zipper device for different nanobender lengths and extract the displacement at the center of the zipper cavity and at the end of the nanobender. A tether with width 150 nm and length 360 nm is chosen for all following simulations and for device fabrication. Supplementary Figure 6a shows the displacement as a function of the nanobender length L. The zipper cavity is deformed by the nanobenders as shown in Fig. 1 of the main text. As a result, The displacement at the center of the zipper cavity (solid lines) is larger than the displacement at the end of the nanobender (dashed lines). Comparing the cases with (blue) and without (red) tether, we observe that while the displacements at the end of the nanobender are nearly identical, the displacement at the center of the zipper cavity is $\sim 10\%$ higher without the tether than with the tether. This can be qualitatively explained by the boundary condition argument. The zipper cavity is forced to bend more without the tether, leading to a larger displacement. In addition, we extract a scaling law of $\Delta \propto L^{1.63}$ for the displacement at the end of the nanobender. The displacement at the center of the zipper cavity approaches this scaling law for longer nanobender length L.

To illustrate the potential importance of the tether, we also simulate nanobenders with different lengths attached to a rigid cavity. The rigid cavity is approximated by a block with the same thickness and length as the zipper cavity while the width is chosen to be 2 µm such that the in-plane bending of the cavity itself is negligible. The simulated

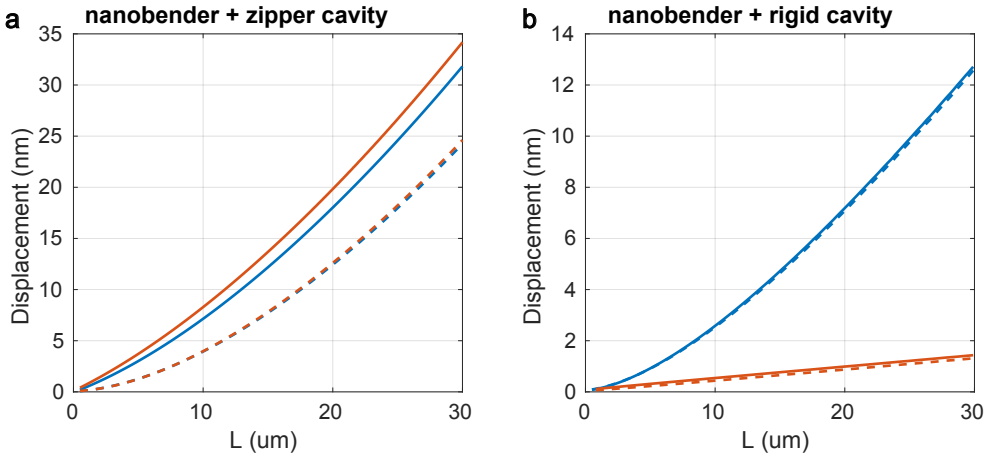

Supplementary Figure 6. **Comparison of displacement with and without the tether.** **a**, Simulated displacement of a bender-zipper cavity versus the nanobender length L. **b**, Simulated displacement of nanobenders attached to a rigid cavity versus L. Solid lines show the displacement at the center of the cavity. Dashed lines show the displacement at the end of the nanobender. Blue (red) color represents device with (without) tether between the nanobender and the cavity.

displacement is shown in Supplementary Figure 6b. We clearly observe that the displacement at the center of the cavity is nearly identical to the displacement at the end of the nanobender, as expected for a rigid cavity. Furthermore, adding the tether improves the displacement at the cavity by nearly an order of magnitude. We would like to point out that the difference between tethered and untethered depends on the tether geometry which is constrained by fabrication limitations in our devices.

Supplementary Note 5. OPTICAL BACKGROUND REMOVAL

In this section, we describe how we remove wavelength-dependent background fluctuations in optical reflection measurements that involve DC tuning. These fluctuations arise in the measurement setup and are not part of the actual device response. An example of raw DC tuning measurement data is shown in Supplementary Figure 7a. Even though it is still possible to see tuning of the mode, the background makes it difficult to process the data. Additionally, modes that are very weakly coupled can be hidden by the background. To remove the fluctuations in the background we use the fact that the resonance wavelength of the mode tunes with voltage whereas the background is static. For each wavelength, we can thus take the mean of the reflection over the DC voltages. Formally, for a reflection r_{ij} at wavelength i and voltage j, we compute the mean $m_i = \frac{1}{M}\sum_j r_{ij}$ where M is the number of voltages. We then normalize the reflection $r_{ij,\text{norm}} = r_{ij}/m_i$ and recover the plot shown in Supplementary Figure 7b. The fluctuating background is removed whereas the tunable modes are not affected. In Supplementary Figure 7c we show a comparison of the raw and normalized reflection spectrum at 0 V and see that the normalized background is flat. Because the control optical mode is static, we expect it to be removed through normalization. However, it is still visible, although slightly distorted. By looking at the control mode more carefully, we observe that it is slightly drifting with time as the experiment is being carried on, which means it is not perfectly static. Looking at a close up of one of the tunable modes (Supplementary Figure 7d), we see that neither the wavelength nor the linewidth of the mode are affected by the background removal.

Supplementary Note 6. ROTATED NANOBENDERS

We have considered Y-cut LN where the nanobender is parallel to the crystal X axis. In this section we investigate how changing the in-plane orientation of the nanobender affects the displacement $\boldsymbol{u}$ of the nanobender. This amounts to changing the angle φ between X and x (parallel to the nanobender), where X is the crystal axis, x is the global coordinate fixed with the nanobender and is pointing from the fixed-end towards the free-end of the nanobender. Global z axis is perpendicular to the chip (parallel to crystal Y axis).

A good indicator for how the displacement varies with φ is to look at how the rotated piezoelectric components d_{21} and d_{31} change with φ (Supplementary Figure 8a). As discussed in Supplementary Note 1, d_{21} (d_{31}) couples

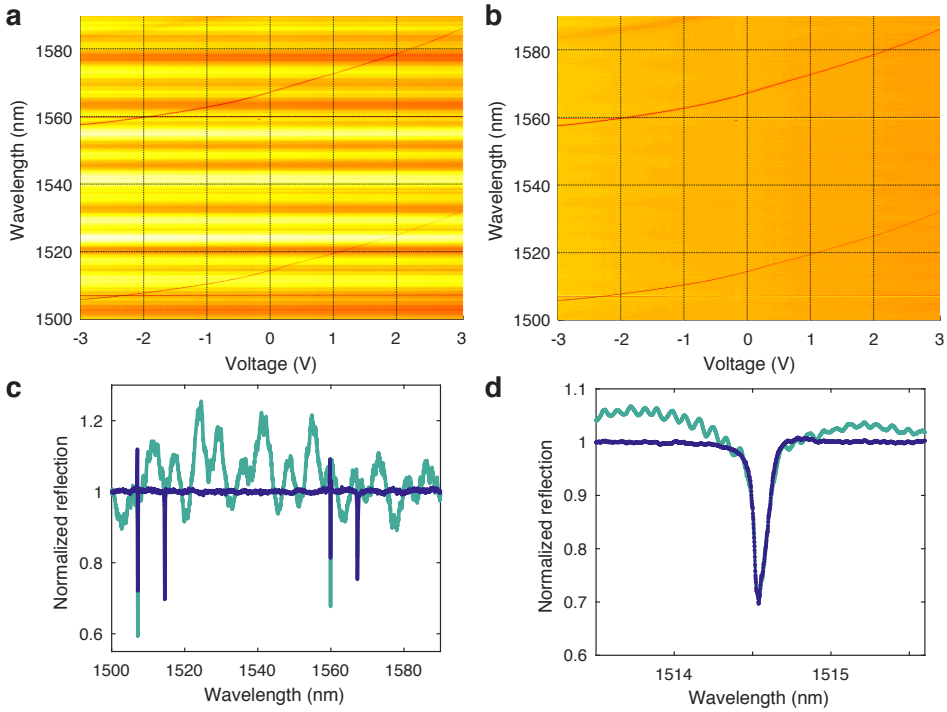

Supplementary Figure 7. **Optical background removal in the presence of a tunable mode.** **a**, Raw measurement. **b**, Normalized measurement with background removal. **c**, Line-cut of (a) and (b) at 0 V. **d**, Close-up of (c) around the fundamental optical mode of the active zipper cavity.

between E_y (E_z) and S_{xx}, and generates vertical (horizontal) bending from $\partial_z E_y$ ($\partial_y E_z$). We can directly compare it to simulated displacements of a nanobender with $L = 10\,\mu\text{m}$ where φ is swept from 0 to 2π.

Plotting the maximal and minimal value of the displacement (Supplementary Figure 8b), we see that the out-of plane component u_z varies approximately as d_{21}. The in-plane displacement component perpendicular to the nanobender u_y follows d_{31} relatively well when φ is changed, although the resulting curves are asymmetric. We attribute this to one end of the nanobender being anchored, breaking the symmetry, and also contributions from other non-zero piezoelectric components. When $\varphi = 90°$, we see that the in-plane displacement u_y is reduced by a factor 4.5. Moreover, for a bender-zipper cavity, two nanobenders rotated by $\pm 90°$ are attached to the two ends of the same half of the zipper cavity. The two nanobenders would bend towards opposite directions (Supplementary Figure 8b, at $\pi/2$ and $3\pi/2$) if they were not connected, leading to a small net displacement. From simulations of a rotated bender-zipper cavity, we find that u_y decreases by more than one order of magnitude.

We fabricate and measure such a bender-zipper cavity where $\varphi = 90°$. The device (Supplementary Figure 8c) does not have a waveguide with a 90° bend as opposed to the bender-zipper cavity aligned along crystal axis X in the main text. Moreover the nanobenders are attached to the zipper cavity through small tethers. We confirm that the active bender-zipper cavity is free to move by measuring its thermal-mechanical power spectral density (Supplementary Figure 8d) which looks typical of previously measured tunable devices. As expected, the DC tuning measurement of the rotated device (Supplementary Figure 8e and f) shows only little tuning. We extract a DC tuning coefficient of $\alpha \sim 0.04\,\text{nm}\,\text{V}^{-1}$ which is significantly smaller than devices with $\varphi = 0$ where we measure $\alpha \sim 1\,\text{nm}\,\text{V}^{-1}$. Moreover, we measure that the control zipper cavity does not tune at all.

Lastly it is worth noting that according to the simulation results, a variety of actuation directions can be achieved with the same crystal cut by fabricating the nanobender along different in-plane orientations. For example, relatively clean vertical actuation can be achieved at $\varphi \approx 270 \pm 20$ degrees even on Y-cut LN.

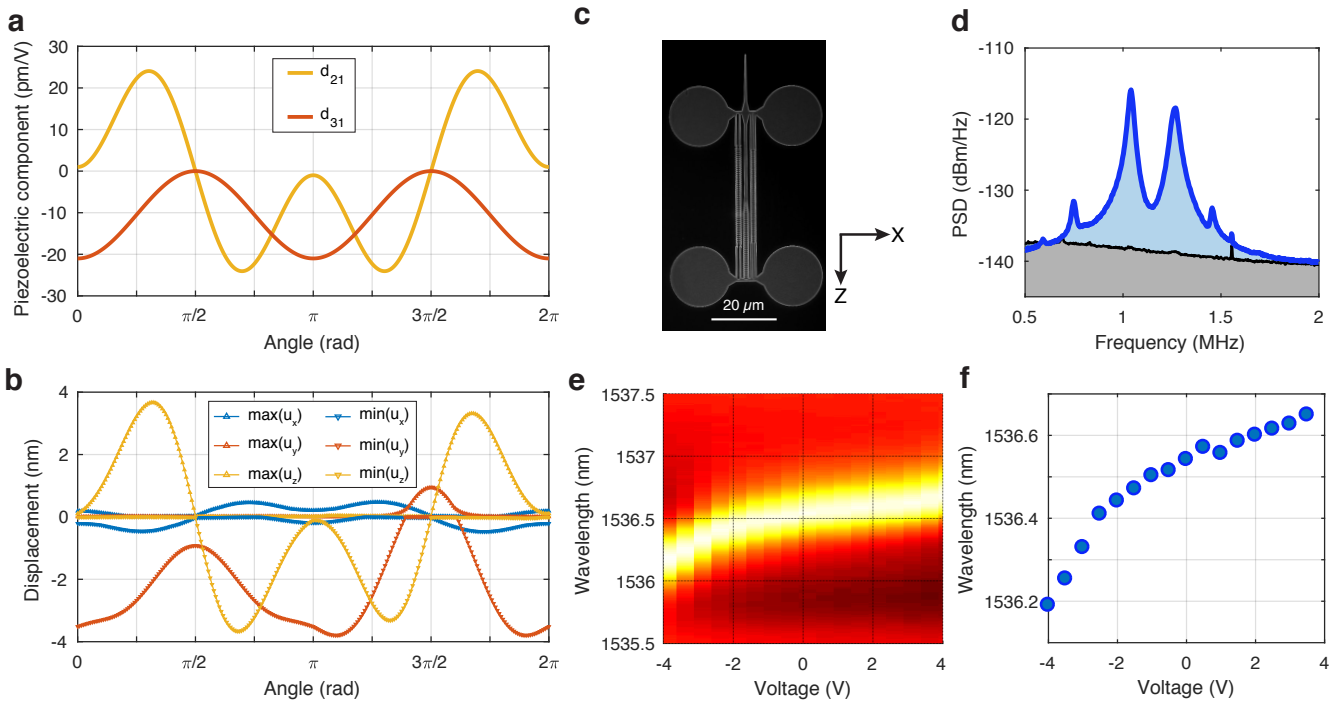

Supplementary Figure 8. **Bender-zipper cavity aligned along crystal axis Z.** **a**, Piezoelectric components for Y-cut lithium niobate versus angle between global axis x and crystal axis X. **b**, Simulated displacement of a nanobender versus nanobender orientation. An angle of 0° (90°) corresponds to the nanobender parallel to crystal axis X (Z). **c**, Scanning electron micrograph of a bender-zipper cavity aligned along crystal axis Z (taken before the aluminum evaporation). **d**, Thermal power spectral density of the rotated bender-zipper cavity. **e**, Measured DC tuning of the fundamental optical mode of a rotated bender-zipper cavity attached to $L = 10\,\mu$m nanobenders through narrow tethers. The background is removed through normalization. **f**, Wavelength tuning as a function of voltage. The data is extracted from Supplementary Figure 8e. Error bars are smaller than the marker size in the plot.

Supplementary Note 7. LOW TEMPERATURE AND PRESSURE MEASUREMENTS

A. Thermal broadening

In this section, we show that the optical linewidths of the bender-zipper cavities are limited by thermal-mechanical broadening at room temperature. This effect causes the Lorentzian lineshape of the resonance to be convoluted by a Gaussian distribution representing the random position of the mechanical degree of freedom due to Brownian motion. The resulting profile is the so-called Voigt profile [6]. If the linewidth of the Gaussian $\kappa_{\rm G}$ is much larger than the linewidth of the cavity resonance κ, then the linewidth of the Voigt profile is

$$\kappa_{\rm V} \approx \kappa_{\rm G}. \tag{17}$$

To compute this broadened linewidth $\kappa_{\rm G}$, we proceed with calculating the root mean square displacement $x_{\rm rms}$ caused by thermal Brownian motion. We consider one half of a $L = 7\,\mu$m bender-zipper cavity. By simulating the displacement profile of the fundamental mechanical in-plane mode, we calculate the effective motional mass associated with it through [5]:

$$m_{\rm eff} = \frac{\int dV \rho(\mathbf{x})|\mathbf{u}(\mathbf{x})|^2}{\max|\mathbf{u}(\mathbf{x})|^2} = 10.5 \text{ pg}.$$

Here, $\rho(\mathbf{x})$ is the density of the material and $\mathbf{u}(\mathbf{x})$ is the displacement field. This mechanical mode has a frequency $\Omega_{\rm m}/2\pi = 1.04$ MHz. Using the equipartition theorem, we find [6]:

$$x_{\rm rms,h} = \sqrt{\frac{k_B T}{m_{\rm eff}\Omega_{\rm m}^2}} = 95 \text{ pm}.$$

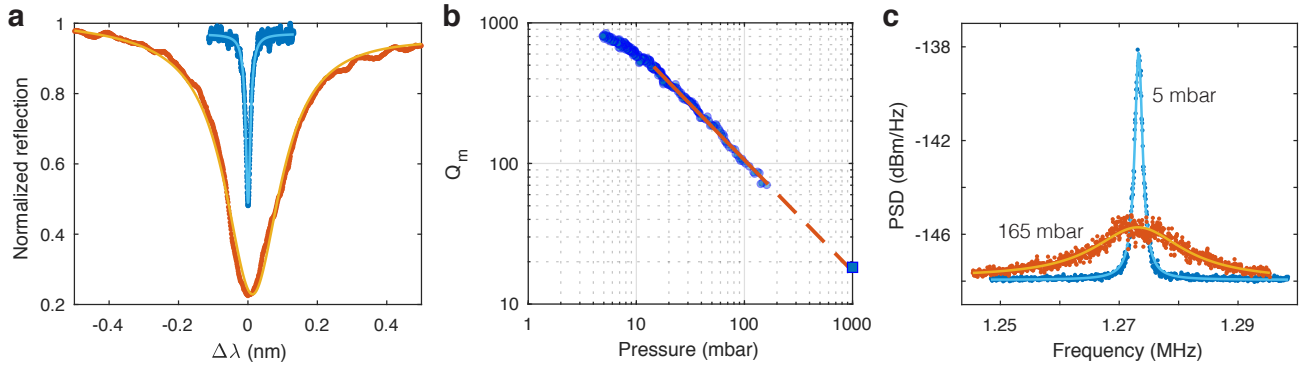

Supplementary Figure 9. **Low temperature and low pressure measurements.** **a**, Room temperature (red) and low temperature (blue) optical reflection spectrum of a bender-zipper cavity. The spectrum is fitted with a Lorentzian function to extract the linewidth in both cases. When the temperature is lowered, the mode is blue-shifted due to thermal contraction of the cavity. This shows that the optical mode is thermally broadened at room temperature. **b**, Q of a thermal mechanical resonance as a function of pressure at room temperature (blue circles). The red line is a fit, which when extrapolated (dashed red) to 1000 mbar agrees well with a measurement performed outside of the vacuum chamber (blue square). Error bars are smaller than the marker size in the plot. **c**, Thermal power spectral density of one of the mechanical resonances at two different pressures. We use a Lorentzian function to fit the curves. Notice the narrowing of the mode at lower pressure due to reduced air damping.

Here, $T = 293$ K is the room temperature and k_B is the Boltzmann constant. The root mean square displacement of the full bender-zipper cavity is then simply given by: $x_{\mathrm{rms}} = \sqrt{2}x_{\mathrm{rms,h}} = 134$ pm. From optical resonance wavelength versus zipper cavity gap size simulations (Supplementary Figure 5e), we extract the optomechanical coupling $G_{\mathrm{OM}}/2\pi \approx 42\,\mathrm{GHz\,nm^{-1}}$. This value assumes a gap size of ~ 100 nm. Finally, the broadened linewidth is given by [6]:

$$f_G = 2\sqrt{2\ln(2)} \cdot \frac{G_{\mathrm{OM}}}{2\pi}\frac{\lambda^2}{c}x_{\mathrm{rms}} = 108 \text{ pm}.$$

At a temperature of 4 K, the same expression leads to $f_G = 13$ pm. We therefore expect the linewidth of the cavity to decrease at low temperatures if it is limited by thermal broadening.

In Supplementary Figure 9a we compare the measured reflection spectrum of a tunable bender-zipper cavity at room temperature and in a ~ 4 K cryostat. We observe that the linewidth decreases from 194 pm to 16 pm when cooling down which is more than an order of magnitude. The room temperature linewidth is on the same order as the theoretically predicted broadening. Because the gap $\tilde{g}_0$ is difficult to accurately measure, so is estimating G_{OM}. This could help explain the difference between predicted and measured values for the broadened linewidth. Additionally, simulating the full bender-zipper cavity as well as taking into account more mechanical modes that lead to broadening could help compute a more accurate value for the linewidth. In the low temperature case, f_G is comparable to κ and so equation 17 does not hold anymore. Moreover, the resonance wavelength gets blue-shifted from 1534 nm to 1521 nm when cooling down which is expected from thermal contraction and refractive index change. The measured bender-zipper cavity has a gap $\tilde{g}_0 \approx 100$ nm which we extract from a scanning electron micrograph taken before release. The device was cooled down using a closed-cycle Montana Instruments cryostat.

Finally, we compute the zero-point fluctuation for the full bender-zipper cavity which is given by [5]:

$$x_{\mathrm{zpf}} = \sqrt{2}\sqrt{\frac{\hbar}{2m_{\mathrm{eff}}\Omega_{\mathrm{m}}}} \approx 39 \text{ fm}.$$

This allows us to obtain the vacuum optomechanical coupling strength $g_0 = G_{\mathrm{OM}} \cdot x_{\mathrm{zpf}} \approx 2\pi \times 1.6$ MHz.

B. Mechanical quality factor as a function of pressure

We investigate how the thermal-mechanical power spectrum of the bender-zipper cavity changes when pressure is decreased. At atmospheric pressures, the mechanical quality factor $Q_{\mathrm{m}} \approx 18$ is limited by air damping. We use the cryostat from the previous section as a vacuum chamber at room temperature and measure the thermal-mechanical spectrum as the chamber is being pumped down. We extract Q_{m} as a function of pressure (Supplementary Figure 9b

and c). As the pressure decreases, the quality factor increases at a slightly sub-linear rate. We observe a two-order of magnitude increase in the mechanical quality factor, reaching $Q_\mathrm{m} \sim 1000$ at 5 mbar. Extrapolating this rate to atmospheric pressure at 1000 mbar agrees well with measurement. Below ~ 10 mbar, we can see Q_m start saturating, showing that air damping is no longer the main mechanism for dissipation. Thermo-elastic damping starts becoming dominant at room temperature and low pressure, so we expect Q_m to further improve at low temperature.

Supplementary Note 8. MECHANICAL MODE FREQUENCY AND AC MODULATION MEASUREMENT

A. Fundamental mechanical mode frequency as a function of nanobender length

In this section, we study the actuation speed of a single nanobender as well as the tuning speed of the bender-zipper cavity. For the case of a single nanobender, Euler-Bernoulli beam theory allows us to write a simple expression for its fundamental eigenfrequency. The in-plane fundamental eigenfrequency of a beam clamped on one side, is given by [7]

$$\begin{aligned} f_1 &\approx \frac{3.5161}{2\pi L^2}\sqrt{\frac{EI}{\mu}} \\ &= \frac{3.5161}{2\pi}\sqrt{\frac{E}{12\rho}}\frac{w}{L^2} \end{aligned}$$

where E is Young's modulus, $I = \frac{tw^3}{12}$ is the second moment of area and $\mu = \rho w t$ is the mass per unit length. The density of LN is $\rho = 4700\,\mathrm{kg\,m^{-3}}$. The agreement with finite element method simulations (see Supplementary Figure 10a) is very good, overestimating the actual values by only $\sim 5\%$. This deviation arises because the analytical expression is not taking into account the anisotropy of LN (we approximated LN as an isotropic material and took $E \approx 2.03 \cdot 10^{11}$ Pa [8]). Furthermore, the analytical expression does not include the aluminum electrodes which would decrease the frequency due to the much smaller Young's modulus of aluminum. We can recover the spring constant of the nanobender: $k = 4\pi^2 \mu L f_1^2 \approx 5.7\,\mathrm{N\,m^{-1}}$ for $L = 10\,\mu\mathrm{m}$. This lets us convert the displacement actuation to an equivalent force per volt of $F/U = k\Delta/U \approx 5.7\,\mathrm{N\,m^{-1}} \cdot 3.5\,\mathrm{nm\,V^{-1}} \approx 20\,\mathrm{nN\,V^{-1}}$. Because k scales as L^{-3} and Δ/U scales as L^2, the force per volt scales as L^{-1}.

In Supplementary Figure 10a, we also show the simulated fundamental resonance frequency of one half of a bender-zipper cavity as a function of the nanobender length L. As expected, for small L, the nanobender is not limiting the tuning speed of the cavity but rather the size of the cavity itself. In Supplementary Figure 10b, we compare this simulated curve to experimental values obtained from thermal mechanical spectra of 21 bender-zipper cavities. For each device, we observe multiple resonance frequencies which are spread around the curve obtained from simulation. Simulating the full structure should lead to a splitting of the resonance frequency due to the mechanical coupling between the two identical halves of the bender-zipper cavity.

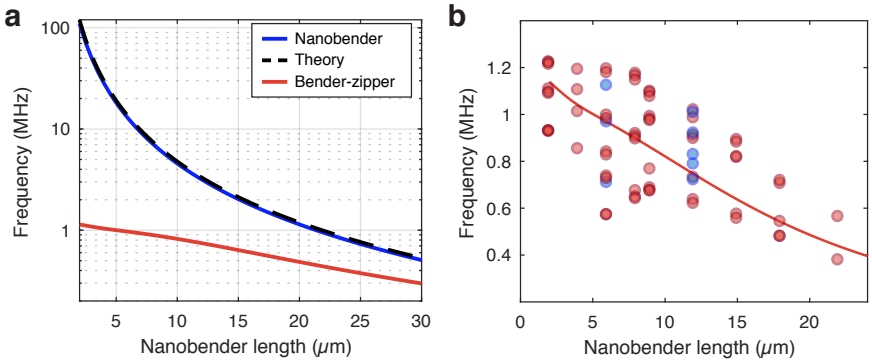

Supplementary Figure 10. **Mechanical resonance frequencies.** **a**, Finite element method simulation of the eigenfrequencies of a nanobender only (blue) and a bender-zipper cavity (red). The dashed black curve is calculated from Euler-Bernoulli beam theory. **b**, Measurement of the resonance frequencies of 21 bender-zipper cavities with varying nanobender lengths L. Devices without and with tether (blue and red circles) are plotted. The red line is the same as the one in Supplementary Figure 10a. Error bars are smaller than the marker size in the plot.

B. AC wavelength shift as a function of modulation voltage

Here, we experimentally confirm that the AC wavelength shift $\Delta\lambda_{ac}$ of the bender-zipper cavity is linear with respect to the driving voltage V_{ac}. In Supplementary Figure 11a, we show results of modulation experiments where we sweep V_{ac} from 0 to 50 mV. This measurement is done for two different resonance frequencies of the bender-zipper cavity (see Fig. 3e in the main text). We proceed as in the main text and extract $\Delta\lambda_{ac}$ as a function of V_{ac} by doing an analytical fit and converting bias voltage to wavelength. These are plotted in Supplementary Figure 11b. By fitting a line, we extract the AC tuning coefficient for a specific resonance frequency. We find that the AC tuning coefficient is independent of V_{ac} for the range of voltages considered here, validating the voltage normalization done in Fig. 3e of the main text.

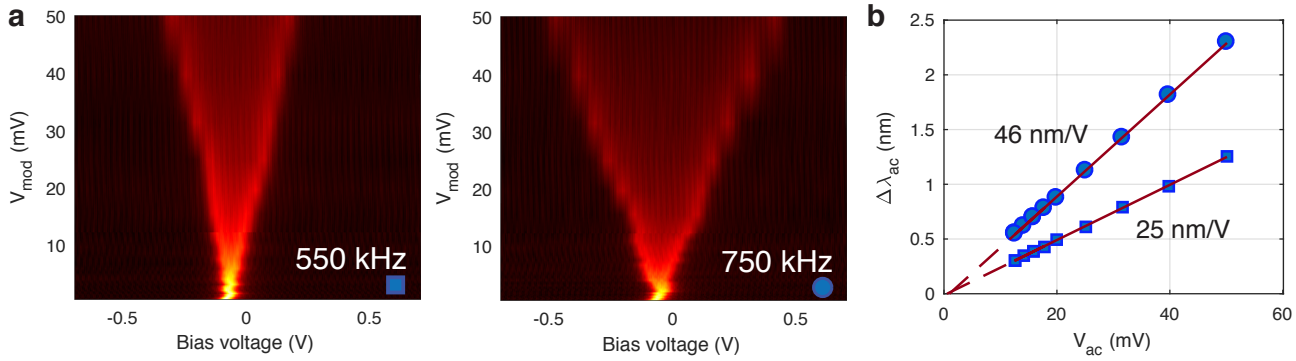

Supplementary Figure 11. **Sweeping the AC voltage applied to a bender-zipper cavity.** **a**, Modulation measurement results for two different modulation frequencies corresponding to two different mechanical resonances. The device measured here is the same as the one in Fig. 3c in the main text. **b**, Analytical fit (blue circles) of both modulation measurements shown in Supplementary Figure 11a. As explained in the main text, bias voltage is converted to wavelength shift. The red line is a linear fit. Error bars are smaller than the marker size in the plot.

Supplementary Note 9. APPROXIMATED DISPLACEMENT FOR ZIGZAG NANOBENDERS

In this section, we show that the nanobender on Y-cut LN can be wrapped in a zigzag structure without metal crossover while maintaining efficient displacement actuation. The direction of the in-plane displacement can be controlled by the aspect ratio of the zigzag structure. Furthermore, the identical zigzag configuration generates out-of-plane deflection that accumulates along the zigzag on Z-cut LN.

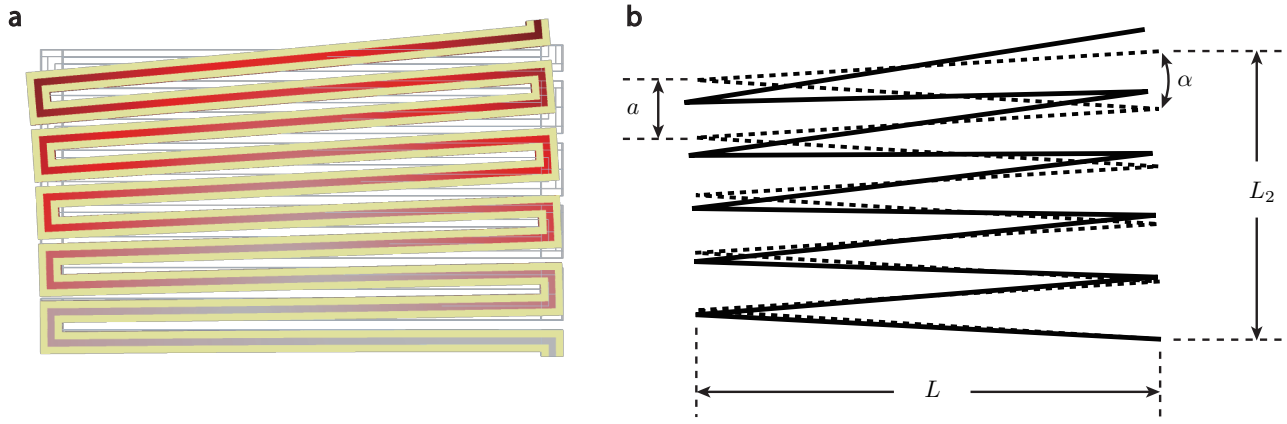

Supplementary Figure 12. **Zigzag nanobenders on Y-cut lithium niobate for in-plane displacement.** **a**, Simulated displacement for a zigzag nanobender. The bottom-right corner of the zigzag structure is fixed. The LN domain is colored by displacement and the electrodes are colored in yellow. **b**, Simplified geometry of the zigzag nanobender. The geometry at equilibrium is shown as dashed lines, and the deformed geometry is shown as solid lines.

Supplementary Table 2. Simulated and estimated one-volt displacement for Y-cut zigzag nanobenders.

N	L (µm)	L_2 (µm)	Simulated $\boldsymbol{u}$ (nm)	Estimated $\boldsymbol{u}$ (nm)
10	4	13	$(53.4, 20.6, 0.14)$	$(49.5, 15.2, 0)$
2	15	2.6	$(7.3, 46.8, 0.37)$	$(7.4, 42.8, 0)$
5	10	6.5	$(31.6, 54.1, 0.30)$	$(30.9, 47.6, 0)$

We start with a Y-cut zigzag nanobender. Supplementary Figure 12 shows a simulated displacement profile (Supplementary Figure 12a) and a schematic drawing of the simplified zigzag geometry (Supplementary Figure 12b). We simplify one unitcell of the zigzag structure as two solid lines which connect at the "U-turns" and form an angle $\alpha = 2\arctan(a/2L) \approx a/L$. L is the length of a single nanobender and a is the width of one unitcell. The extension of the zigzag structure is $L_2 \equiv Na$ where N is the number of unit cells.

Since only the in-plane displacements are relevant, the coordinates and displacements can be represented by complex numbers. We establish a complex plane such that the real axis is parallel to a single nanobender and the origin coincides with the bottom right of the zigzag structure where it is anchored. To move along the vertices of the simplified zigzag, two complex numbers $v_1 = -L + ia/2$ and $v_2 = L + ia/2$ can be added consecutively. As a result, for a zigzag nanobender with N unit cells ($2N$ connected nanobenders), the position of the end point x_N is

$$x_N = N(v_1 + v_2) = iNa. \tag{18}$$

When a voltage is applied such that a single nanobender is deflected by an angle θ as defined in Supplementary Note 1, it will be shown in the following that the displacement at x_N is solely determined by θ, L and L_2.

As shown in Supplementary Figure 1, every nanobender in the zigzag structure contributes a rotation of $\exp(i\phi)$ from one vertex to the next vertex. Note that the rotation is $\phi = 2\theta$ instead of θ. One would expect θ if only considering the displacement. However, the next nanobender is connected tangentially to the end of the previous nanobender, which, due to the bending, has changed its orientation by ϕ. The end position x'_N of the zigzag after the series of bending and rotation can be expressed as

$$\begin{aligned} x'_N &= v_1 e^{i\phi} + v_2 e^{2i\phi} + \cdots + v_1 e^{(2N-1)i\phi} + v_2 e^{2Ni\phi} \\ &= \left(v_1 e^{i\phi} + v_2 e^{2i\phi}\right) \sum_{k=0}^{N-1} \exp(2ik\phi) \\ &= \left(v_1 + v_2 e^{i\phi}\right) \frac{\sin(N\phi)}{\sin\phi} e^{iN\phi}. \end{aligned} \tag{19}$$

The resulting displacement at the end of the zigzag is

$$\begin{aligned} u_N \equiv x'_N - x_N &\approx (v_1 + v_2(1 + i\phi)) \cdot N \cdot (1 + iN\phi) - (v_1 + v_2) \cdot N \\ &\approx (v_1 + v_2) \cdot N \cdot iN\phi + i\phi v_2 N \\ &= N\phi \cdot (-aN + iv_2) \approx N\phi(-L_2 + iL). \end{aligned} \tag{20}$$

We have expanded the expression up to first order in ϕ, used the relationship $v_1 + v_2 = ia$ and the approximation $v_2 = L + ia/2 \approx L$. Written back in vector notation, we obtain the in-plane displacement

$$\boldsymbol{u}_N = N\phi(-L_2, L) = CNL(-L_2, L), \tag{21}$$

where C is the bending curvature that can be obtained by a single nanobender simulation, which is much faster than simulating the full zigzag structure. The total displacement is enhanced by the number of unit cells N, and the direction of the displacement is related to the overall geometry of the zigzag structure L and L_2.

To compare the above simplified estimation to the simulated displacement, we evaluated the maximal displacements from three different zigzag structures using COMSOL and using the estimation Eq. 21. The comparison is shown in Supplementary Table 2. A one-volt curvature of $C = 95.2\,\mathrm{m}^{-1}$ obtained from a single nanobender simulation is used. We see reasonable agreement between simulated and estimated displacements for zigzags with various aspect ratios L/L_2, where the deviations are all $\lesssim 20\%$.

When Z-cut zigzag nanobenders are considered for out-of-plane actuation, the situation is simpler comparing to the Y-cut in-plane zigzag nanobenders. The direction of bending is disentangled with the geometry of the zigzag structure, and the rotation simply accumulates along the zigzag structure (Supplementary Figure 13).

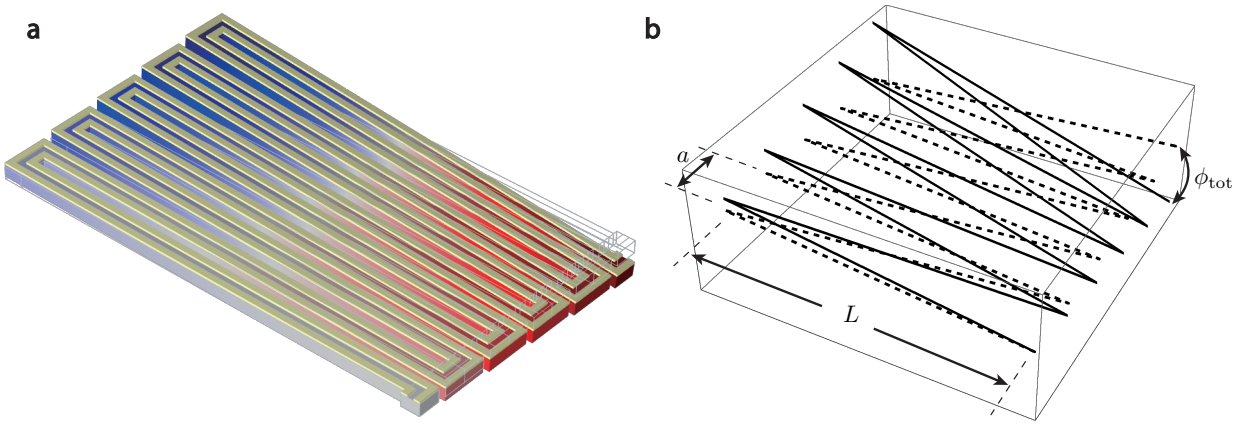

Supplementary Figure 13. **Zigzag nanobenders on Z-cut LN for out-of-plane deflection. a**, Simulated displacement for a zigzag nanobender. The bottom-right corner of the zigzag structure is fixed. The LN domain is colored by the out-of-plane displacement and the electrodes are colored in yellow. **b**, Simplified geometry of the zigzag nanobender. The geometry at equilibrium is shown as dashed lines, and the deformed geometry is shown as solid lines.

More specifically, at the end of each unit cell of the deformed zigzag, the tangential direction is changed by 2ϕ. After N unit cells, the accumulated angle is $\phi_{\rm tot} = 2N\phi = 2NCL$ where C is the bending curvature. For a one-volt $C \sim 100\,\mathrm{m}^{-1}$, $L = 20\,\mu\mathrm{m}$ and $N = 10$, $\phi_{\rm tot} \sim 0.04 = 2.3$ degrees. A deflection of ± 23 degrees can be achieved with voltages between $\pm 10\,\mathrm{V}$.

As for the corresponding vertical displacement, it is directly given by $\Delta_{zz} \approx \phi_{\rm tot} L/2 = NCL^2$. This is much smaller than the displacement generated by a single nanobender with the same total length $L_{\rm tot} = 2NL$, which is $\Delta \approx CL_{\rm tot}^2/2 = 2N^2CL^2$. Since a large displacement is transduced, one expects the effective stiffness of the single nanobender with length $L_{\rm tot}$ to be much smaller than the zigzag structure. To verify this, we simulated the displacement of a zigzag nanobender with $L = 10\,\mu\mathrm{m}$ and $N = 5$ under a vertical force of $f_v = 1\,\mathrm{nN}$ at the end of the zigzag, and also the displacement of a single nanobender with $L_{\rm tot} = 100\,\mu\mathrm{m}$ under the same conditions. The simulated displacements are $\Delta_{zz} = 27.6\,\mathrm{nm}$ for the zigzag and $\Delta = 1.5\,\mu\mathrm{m}$ for the single nanobender.

From Euler-Bernoulli beam theory (see also Supplementary Note 8 A), the effective spring constant of a beam scales as $k \propto L^{-3}$. By approximating the joint between every nanobenders in the zigzag structure as a stiff connection, the effective spring constant of the zigzag is $k_{zz} \propto L^{-3}/(2N)$, where the proportionality coefficient is determined by material properties and the cross section geometry. On the other hand, the single nanobender has $k \propto L_{\rm tot}^{-3} = L^{-3}/(2N)^3$. As a result, the single nanobender is a factor of $4N^2$ less stiff than the zigzag nanobender. Note that the central angle generated by the single nanobender is $\phi = CL_{\rm tot} = 2NCL$, identical to the zigzag nanobender. Hence for applications where an out-of-plane rotation is desired, the zigzag nanobender is advantageous over a single nanobender, where the zigzag nanobender generates an identical out-of-plane rotation with a much stiffer structure.

SUPPLEMENTARY REFERENCES

[1] Zubko, P., Catalan, G. & Tagantsev, A. K. Flexoelectric effect in solids. *Annu. Rev. Mater. Sci.* **43** (2013).
[2] Bhaskar, U. K. *et al.* A flexoelectric microelectromechanical system on silicon. *Nat. Nanotechnol.* **11**, 263–266 (2016).
[3] Cordero-Edwards, K., Kianirad, H., Canalias, C., Sort, J. & Catalan, G. Flexoelectric fracture-ratchet effect in ferroelectrics. *Phys. Rev. Lett.* **122**, 135502 (2019).
[4] Jiang, W. *et al.* Lithium niobate piezo-optomechanical crystals. *Optica* **6**, 845–853 (2019).
[5] Chan, J. *Laser cooling of an optomechanical crystal resonator to its quantum ground state of motion.* Ph.D. thesis, California Institute of Technology (2012).
[6] Winger, M. *et al.* A chip-scale integrated cavity-electro-optomechanics platform. *Opt. Express* **19**, 24905–24921 (2011).
[7] Cleland, A. N. *Foundations of nanomechanics: from solid-state theory to device applications* (Springer Science & Business Media, 2013).

[8] Weis, R. & Gaylord, T. Lithium niobate: summary of physical properties and crystal structure. *Appl. Phys. A* **37**, 191–203 (1985).